Baghdad Science Journal

Volume 23 | Issue 1 Article 5

1-1-2026

# Effect of Demineralization and Physical Activation in Enhancing the Porosity and Adsorption Properties of Recovered Carbon Black Pyrolyzed From Waste Tire

Siti Nuramirah Rabbani Muhammad Zaki
*Faculty of Applied Sciences, Universiti Teknologi MARA (UiTM), Cawangan Selangor, Kampus Shah Alam, Selangor, Malaysia*, nurbani9600@gmail.com

Nurul Fatahah Asyqin Zainal
*Centre of Foundation Studies, Universiti Teknologi MARA (UiTM), Cawangan Selangor, Kampus Dengkil, Selangor, Malaysia AND RIG Sustainability Material Design and Manufacturing, Universiti Teknologi MARA (UiTM), Selangor, Malaysia*, nurulfa2916@uitm.edu.my

Hartini Ahmad Rafaie
*Centre of Foundation Studies, Universiti Teknologi MARA (UiTM), Cawangan Selangor, Kampus Dengkil, Selangor, Malaysia*, hartinirafaie@uitm.edu.my

Suhaila Idayu Abdul Halim
*RIG Sustainability Material Design and Manufacturing, Universiti Teknologi MARA (UiTM), Selangor, Malaysia AND Eco Power Synergy Sdn. Bhd., Bandar Puchong Jaya, Selangor, Malaysia*, suhailaidayu@gmail.com

Chia Chay Tay
*Faculty of Applied Sciences, Universiti Teknologi MARA (UiTM), Cawangan Selangor, Kampus Shah Alam, Selangor, Malaysia; RIG Sustainability Material Design and Manufacturing, Universiti Teknologi MARA (UiTM), Selangor, Malaysia AND myBioREC, School of Civil Engineering, College of Engineering, Universiti Teknologi MARA (UiTM), Selangor, Malaysia*, taychiay@staf.uitm.edu.my



How to Cite this Article
Zaki, Siti Nuramirah Rabbani Muhammad; Zainal, Nurul Fatahah Asyqin; Rafaie, Hartini Ahmad; Halim, Suhaila Idayu Abdul; and Tay, Chia Chay (2026) "Effect of Demineralization and Physical Activation in Enhancing the Porosity and Adsorption Properties of Recovered Carbon Black Pyrolyzed From Waste Tire," *Baghdad Science Journal*: Vol. 23: Iss. 1, Article 5.
DOI: https://doi.org/10.21123/2411-7986.5136

BAGHDAD SCIENCE JOURNAL 2026;23(1):55–70



SPECIAL ISSUE ARTICLE

# Effect of Demineralization and Physical Activation in Enhancing the Porosity and Adsorption Properties of Recovered Carbon Black Pyrolyzed From Waste Tire

**Siti Nuramirah Rabbani Muhammad Zaki** [1], **Nurul Fatahah Asyqin Zainal** [2,3,*], **Hartini Ahmad Rafaie** [2], **Suhaila Idayu Abdul Halim** [3,5], **Chia Chay Tay** [1,3,4]

[1] Faculty of Applied Sciences, Universiti Teknologi MARA (UiTM), Cawangan Selangor, Kampus Shah Alam, Selangor, Malaysia
[2] Centre of Foundation Studies, Universiti Teknologi MARA (UiTM), Cawangan Selangor, Kampus Dengkil, Selangor, Malaysia
[3] RIG Sustainability Material Design and Manufacturing, Universiti Teknologi MARA (UiTM), Selangor, Malaysia
[4] myBioREC, School of Civil Engineering, College of Engineering, Universiti Teknologi MARA (UiTM), Selangor, Malaysia
[5] Eco Power Synergy Sdn. Bhd., Bandar Puchong Jaya, Selangor, Malaysia

## ABSTRACT

This research aims to improve the porosity structure and adsorption characteristics of rCB through demineralization and physical activation techniques. Hydrochloric acid (HCl) at various concentrations (1, 5, 6, and 10 M) was employed for demineralization, followed by the addition of 6 M potassium hydroxide (KOH). Physical activation was conducted at temperature ranges of 300, 350, 400, 450, and 500°C for durations of 1, 2, and 3 h. Characterization of rCB was conducted using Fourier Transform Infrared Spectroscopy (FTIR), ash content analysis, Inductively Coupled Plasma Optical Emission Spectroscopy (ICP-OES), Brunauer-Emmett-Teller (BET), and iodine adsorption number (IAN). Demineralization decreased the ash content from 11.36% to 8.05% and removed iron ($Fe^{3+}$) and magnesium ($Mg^{2+}$) metals. Conversely, physical activation markedly enhanced the porosity of rCB, attaining a peak BET surface area of 188.52 m2 g-1 and an IAN of 100 mg g-1 at 450°C for 1–2 h. Increased temperatures led to pore collapse, particularly at 500°C. The findings indicate that the optimum temperature and duration of physical activation enhance the structure of rCB. This phenomenon facilitates the widespread use of treatment for environmental remediation, including the treatment of wastewater containing dyes.

**Keywords:** Environmental remediation, Hydrochloric acid, Iodine adsorption number, Potassium hydroxide, Pyrolysis, Surface area

## Introduction

The worldwide disposal of waste tires poses a considerable difficulty, with around 1.5 billion tires discarded annually.[1] Accumulation in landfills contributes to land-use complications, fire hazards,[2] and environmental pollution. Combustion releases volatile organic compounds (VOCs),[3] heavy metals, and polycyclic aromatic hydrocarbons (PAHs).[4] Additionally, chemicals leached from tire rubber, such as N-(1,3-dimethylbutyl)-N'-phenyl-p-phenylenediamine (6PPD) and its toxic derivative 6PPD-quinone, pose serious risks to soil, water, and human health.[5,6] Addressing these issues aligns with Sustainable Development Goals (SDG 12), which promote sustainable waste management through

Received 28 February 2025; revised 25 April 2025; accepted 8 May 2025.
Available online 1 January 2026

* Corresponding author.
E-mail addresses: nurbani9600@gmail.com (S. N. R. M. Zaki), nurulfa2916@uitm.edu.my (N. F. A. Zainal), hartinirafaie@uitm.edu.my (H. A. Rafaie), suhailaidayu@gmail.com (S. I. A. Halim), taychiay@staf.uitm.edu.my (C. C. Tay).

*International Conference on Discoveries in Applied Sciences and Applied Technology (DASAT2025)*
https://doi.org/10.21123/2411-7986.5136

recycling, resource efficiency, and circular economy principles to reduce the environmental impacts of improper tire disposal.[7] Furthermore, it contributes to SDG 13[8] by mitigating climate change, reducing greenhouse gas emissions, and preventing the release of methane ($CH_4$) and carbon dioxide ($CO_2$) from landfilled tires.

Pyrolysis offers an effective solution to recycle waste tires into valuable products, including recovered carbon black (rCB).[9] However, unlike virgin carbon black (vCB), rCB contains residual impurities such as zinc oxide (ZnO) and iron (Fe) that hinder its performance as an adsorbent.[10] Bowles et al.[11] reported rCB has 2.93% sulfur, 5.35% metals, and 6.77% other non-dissolved elements (ONDE), with the most common elements being zinc (Zn) (46.17 g $kg^{-1}$), iron (Fe) (4.08 g $kg^{-1}$), and aluminum (Al) (1.17 g $kg^{-1}$), along with smaller amounts of potassium (K), magnesium (Mg), cobalt (Co), and copper (Cu).

Demineralization effectively reduces impurities in rCB, enhancing its potential use for high-performance materials. This process removes inorganic materials, such as Fe, Zn, sulfur (S), and silicon (Si), by using acidic or basic solutions to purify rCB and pre-activate it for the production of activated carbons (ACs) with improved structural and functional properties. Bowles et al.[11] reported treating rCB with hydrochloric acid (HCl) reduced the ash content of rCB from 16.1% to 5.8–13.1%, increasing its surface area and improving its suitability for adsorption and catalytic applications. Kassahun et al.[12] also reported that demineralization increased the BET surface area to 257 $m^2$ $g^{-1}$, reflecting enhanced porosity.

Physical activation further improves the porosity and surface area of rCB by oxidizing carbon at interstitial sites, thereby creating micropores (<2 nm), mesopores (2–50 nm), and macropores (>50 nm). This process removes carbon as oxides, generating voids that enhance adsorption capabilities via Van der Waals forces. Hou et al.[13] reported that carbon dioxide ($CO_2$) activation increased the surface area from 415 to 733 $m^2$ $g^{-1}$ while maintaining a low ash content of 1.51%. Dziejarski et al.[14] reported that potassium hydroxide (KOH) activation at 900°C increased surface area sixfold and pore volume threefold, with 22% micropores and 78% mesopores contributing to the total pore volume.

Many studies have reported the effective removal of diverse pollutants through the application of adsorption techniques using various materials. Alqadami et al.[15] used hydrochar derived from jackfruit peel and sugarcane bagasse, achieving a high removal capacity of 922.29mg $g^{-1}$ for malachite green due to abundant surface functionalities and well-developed porosity. Azam et al.[16] treated Ajwa date pits with hydrogen peroxide to increase surface polarity and active sites, achieving a Cu(II) adsorption capacity of 1428.57mg $g^{-1}$. Sivasankarapillai et al.[17] developed honeycomb-like nitrogen-doped activated carbon from *Caladium tricolor* leaves, attaining 90 % removal of furazolidone through micropore diffusion and monolayer adsorption. Additionally, Ali et al.[18] synthesized a carboxymethylcellulose-iron nanocomposite that achieved 80 % atorvastatin removal, with adsorption governed by pseudo-first-order kinetics and surface film diffusion.

Despite these advancements, existing literature lacks comprehensive studies on the combined effects of demineralization and/or physical activation on rCB.[12,19,20] Demineralization effectively removes impurities and enhances surface functionality, but its impact on the development of microporous and mesoporous structures remains unclear. On the other hand, while the effects of activation parameters on pore stability and connectivity are well-known, the prior effects of demineralization treatments have not been thoroughly studied. Furthermore, a limited study evaluates the economic viability of these treatments in relation to the rCBs' performance, particularly in terms of their adsorption capacity for environmental remediation.

This study addresses these gaps by providing insight into cost-effective acid–base demineralization supported by detailed cost evaluation and employing low temperature and short duration for physical activation, offering a scalable, energy-efficient, and environmentally sustainable alternative to conventional methods. By evaluating the effectiveness of both approaches, this research provides valuable guidance for optimizing rCB treatment, promoting its development as a high-performance and sustainable adsorbent for environmental applications.

## Materials and methods

### *Preparation of samples*

#### *Demineralization of rCB*

The rCB used in this study was supplied by Eco Power Synergy Sdn. Bhd., Selangor, Malaysia. The rCB samples were obtained from a controlled pyrolysis process, conducted under consistent temperature, duration, and atmospheric conditions, using a standardized feedstock. The sample was first sieved to a uniform particle size of 53$\mu$m, then dried in a conventional oven at 120°C for 24h to remove residual moisture. 4 g of rCB was combined with 100 mL of HCl (ChemAR, Selangor, Malaysia) at concentrations of 1, 5, 6, and 10 M to evaluate the effect of acid

concentration on the properties of rCB. Each mixture was stirred with a magnetic stirrer at 25°C for 1 h. Following the acid treatment, the samples were subjected to vacuum filtration and washed with distilled water at a temperature range of 50–60°C.

Afterward, the rCB samples underwent treatment with 6 M KOH (R&M Chemicals, Manchester, United Kingdom) by repeating the same procedure as the HCl treatment to further eliminate impurities. The KOH-treated samples were vacuum filtered and washed thoroughly with distilled water at 50–60°C until the pH of the filtrate reached 7.0 ± 0.1, indicating neutralization. The demineralized rCB was then dried in a conventional oven at 120°C for 24 h, followed by an additional 24 h of drying in a vacuum oven to ensure complete moisture removal. Among the treated samples, sample D5 (5 M HCl/6 M KOH) exhibited the most optimal properties during demineralization analysis and was selected for further physical activation.

### *Physical activation of demineralized rCB*

The demineralized rCB (sample D5) was further subjected to physical activation in a furnace under an oxygen-free atmosphere, without the use of catalysts, to ensure an inert environment. The samples were placed directly in the furnace and heated to varying temperatures of 300, 350, 400, 450, and 500°C for durations of 1, 2, and 3 h before being cooled to room temperature. Table 1 summarizes the experimental design and the codes assigned to samples treated through demineralization and physical activation.

**Table 1.** Sample codes for demineralization (1, 5, 6, 10M HCl and 6M KOH) and physical activation (300–500°C, 1–3h).

| Treatment | Sample | Code |
|---|---|---|
| No treatment | As received | Raw rCB |
| Demineralization | 0 M HCl/6 M KOH | D0 |
| | 1 M HCl/6 M KOH | D1 |
| | 5 M HCl/6 M KOH | D5 |
| | 6 M HCl/6 M KOH | D6 |
| | 10 M HCl/6 M KOH | D10 |
| Physical activation | 300°C/1 h | D5/AC300-1 |
| | 300°C/2 h | D5/AC300-2 |
| | 300°C/3 h | D5/AC300-3 |
| | 350°C/1 h | D5/AC350-1 |
| | 350°C/2 h | D5/AC350-2 |
| | 350°C/3 h | D5/AC350-3 |
| | 400°C/1 h | D5/AC400-1 |
| | 400°C/2 h | D5/AC400-2 |
| | 400°C/3 h | D5/AC400-3 |
| | 450°C/1 h | D5/AC450-1 |
| | 450°C/2 h | D5/AC450-2 |
| | 450°C/3 h | D5/AC450-3 |
| | 500°C/1 h | D5/AC500-1 |
| | 500°C/2 h | D5/AC500-2 |
| | 500°C/3 h | D5/AC500-3 |

### *Characterization of rCB samples*

*Fourier transform infrared (FTIR) spectroscopy.* The functional groups in rCB were analyzed using Fourier-transform infrared (FTIR) spectroscopy. The analysis was performed in transmittance mode using an FTIR spectrometer (Bruker Alpha Platinum-ATR, Germany) equipped with a diamond crystal window. Spectra were recorded over a range of 4000–500 $cm^{-1}$ with a resolution of 4 $cm^{-1}$. Each measurement consisted of 512 scans conducted at room temperature. Data acquisition and processing were carried out using OPUS software (Bruker, Germany).

*Ash content.* The ash content of rCB was determined in accordance with ASTM D1506-14. The rCB samples were initially dried in a convection oven at 125°C for 1 h and then cooled in a desiccator to prevent moisture absorption. Following drying, crucibles were placed in a muffle furnace at 550 ± 25°C for 1 h and subsequently cooled to room temperature in a desiccator. Approximately 2 ± 0.1 g of dried rCB was placed in each crucible, and the total weight was recorded. The crucibles were placed in a muffle furnace at 550°C for 16 h to ensure complete combustion of the organic components. After combustion, the crucibles were cooled to room temperature in a desiccator, and the constant mass was determined by repeated weighing until no further changes in weight were observed. The ash content was calculated using Eq. (1).

$$A = \left[\frac{D - B}{C - B}\right] \times 100 \quad (1)$$

Where A represented the ash percentage, B was the mass of the crucible (g), C was the mass of the crucible and sample before combustion (g), and D was the combined mass of the crucible and ash after combustion (g).

### *Inductively coupled plasma optical emission spectroscopy (ICP-OES)*

A 0.2 g sample of rCB was placed in a 100 mL polytetrafluoroethylene (PTFE) vessel for elemental analysis, followed by the addition of 10 mL of 68% nitric acid. The microwave digestion process was carried out with sequential heating steps: the sample was heated to 95°C within 3 minutes, held for 5 minutes, then heated to 120°C for another 3 minutes, held for 5 minutes, and finally brought to 130°C and held for 2 minutes to ensure complete metal extraction. The resulting solution was diluted to 50 mL, filtered through a 0.45 $\mu$m cellulose nitrate filter, and analyzed using Inductively Coupled Plasma

Optical Emission Spectroscopy (Avio-500, Perkin Elmer, USA). Blank samples were prepared under the same conditions.[11]

### *Brunauer–emmett–teller (BET)*

The specific surface area of rCB was determined by measuring nitrogen sorption isotherms at 77 K using a surface area and porosity analyzer (BELSORP-mini II, MicrotracBEL, Japan). The surface area and pore volume were calculated using the Brunauer-Emmett-Teller (BET) method. In contrast, the pore size distribution was determined from the adsorption data using the Barrett-Joyner-Halenda (BJH) method.[21,22]

### *Iodine adsorption number (IAN)*

The iodine adsorption number of rCB was determined following ASTM D1510[23] to evaluate the porosity and surface area of rCB. The rCB samples were dried at 125°C for 1 h, then cooled to room temperature and weighed to 0.5 g. Each weighed sample was mixed with an iodine solution and thoroughly agitated using a mechanical shaker. The mixture was subsequently centrifuged, filtered, and titrated against a sodium thiosulfate solution until the solution turned colorless. The iodine adsorption capacity was calculated using Eq. (2):

$$I = \frac{E - S}{E} \times \frac{V}{W} \times N \times 126.91 \quad (2)$$

Where I represented the iodine adsorption number (g $kg^{-1}$), E was the volume ($cm^3$) of sodium thiosulfate required for the blank, S was the volume ($cm^3$) of sodium thiosulfate needed in the sample, V was the calibrated volume of the 25 $cm^3$ iodine pipette (25 mL), W was the weight of the carbon black sample (0.5 g), N was the normality of the iodine solution (meq $cm^{-3}$), and 126.91 was the equivalent mass of iodine (mg $m_{eq}{}^{-1}$).

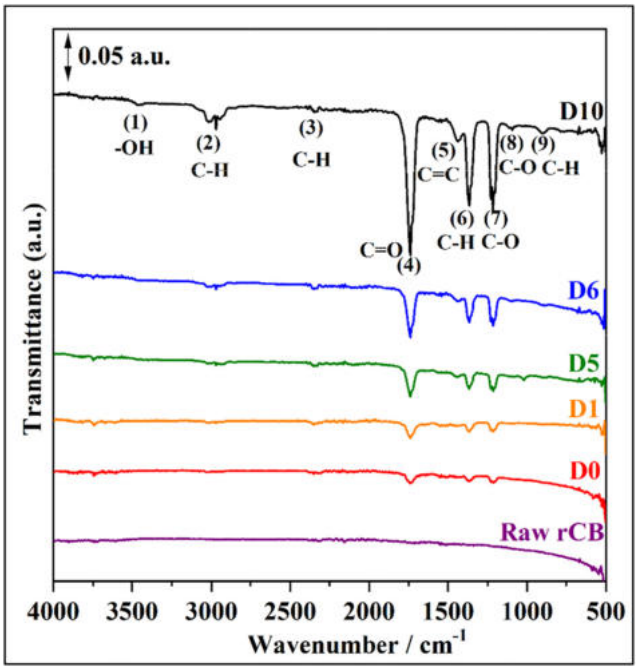


**Fig. 1.** FTIR transmittance spectra of rCB samples treated with varying HCl concentrations followed by 6M KOH at 25°C for 1h.

## Results and discussion

### *Demineralization rCB properties*

### *Fourier transform infrared (FTIR) spectroscopy*

The FTIR spectra of rCB treated with different HCl concentrations (1, 5, 6, and 10 M), followed by KOH treatment, revealed changes in surface functional groups, as shown in Fig. 1 and Table 2.

The FTIR analysis showed that increasing HCl concentration enhanced the removal of surface impu-

**Table 2.** FTIR wavenumber assignments and references for functional group vibrations.

| No. | Wavenumber (s) ($cm^{-1}$) | Reference wavenumber(s) from literature ($cm^{-1}$) | Assignment | Reference |
|---|---|---|---|---|
| (1) | 3600–3200 | 3400<br>3450 | –OH stretching vibration | 10,24–26 |
| (2) | 2920 | 2918 | C–H stretching | 10 |
| (3) | 2850 | 2850 | C–H stretching vibration | 10 |
| (4) | 1700 | 1700 | C=O stretching vibration | 25 |
| (5) | 1570 | 1580<br>1568<br>1632 | C=O stretching vibration | 10,24,26,27 |
| (6) | 1450 | 1400<br>1450 | C=C stretching vibration | 10,24,26 |
| (7) | 1220 | 1100 | C–O stretching vibrations | 10 |
| (8) | 1050 | 1080 | C–O stretching vibrations | 24 |
| (9) | 800–600 | <950 | out-of-plane C–H bending vibrations | 26 |

rities from rCB, effectively exposing reactive sites on the carbon surface. This improved surface treatment facilitates the effect of KOH during the subsequent treatment. Specifically, peaks associated with hydroxyl (-OH) stretching at 3600–3200 $cm^{-1}$ showed a weak but noticeable appearance only at 10 M HCl, indicating the effective removal of impurities by HCl-exposed oxygen-containing functional groups such as carbonyls and epoxides, which facilitated hydroxylation during KOH treatment.[28] The hydroxylation reaction driven by KOH was represented as Eq. (3):

$$C = O + KOH \rightarrow C - OH + K^{+} \quad (3)$$

Peaks attributed to oxygenated functional groups, such as carbonyl (C=O) stretching at 1700$cm^{-1}$ and C–O stretching at 1220 and 1050$cm^{-1}$, became more prominent with increasing HCl concentration in this study, as shown in Fig. 1. These enhancements indicate progressive surface oxidation and removal of inorganic impurities. This is supported by a study that reported the presence of oxygen-containing functional groups, C–O stretching at 1062.44 $cm^{-1}$ upon addition of nitric acid to multi-walled carbon nanotubes (MWCNTs). C–H stretching at 2920$cm^{-1}$ and bending at 1450$cm^{-1}$ vibrations increased with higher acid concentrations due to the exposure of aliphatic hydrocarbon structures following ash and mineral removal.

The aromatic C=C stretching peak at 1570 $cm^{-1}$ also showed increased intensity, reflecting the removal of impurities by HCl, which uncovers and enhances the inherent aromatic structure of rCB.[29] Lastly, the C-H bending in the aromatic region 800–600 $cm^{-1}$ remained consistent across treatments, showing that the core aromatic framework of rCB was preserved despite the extensive surface functionalization.[30] Overall, the increased peak intensities with higher HCl concentrations indicated enhanced oxidation, surface polarity, and functionalization, driven by the synergistic effects of demineralization of HCl and KOH functionalization.

### *Ash content*

Fig. 2 shows the results for ash content analysis of rCB treated at different acid concentrations. When HCl concentration increased, the ash content decreased from 13.96% (raw rCB) to 11.36% (D0), 9.51% (D1), 8.05% (D5), and 7.02% (D6). This is consistent with reported works in the literature. Bowles et al.[12] reported that HCl treatment reduced the ash content of rCB from 16.1% to 5.8–13.1%, while Cardona-Uribe et al.[22] reported a decrease from

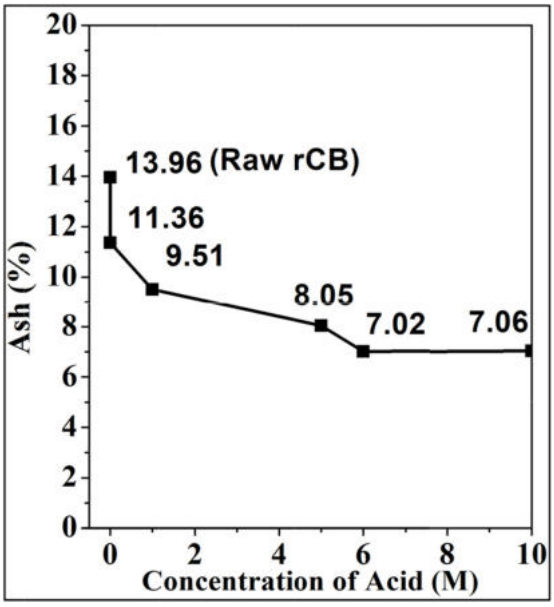


**Fig. 2.** Ash content of rCB treated with varying HCl concentrations followed by 6M KOH at 25°C for 1h.

13.45 wt% to 6.12 wt% with 5 M HCl, both aligning with this trend.

At a 1 M HCl concentration, the acid primarily targeted surface-level contaminants, resulting in a minimum reduction in ash content to 9.51%. At 6 M, the acid diffused deeper into the rCB matrix, effectively dissolving embedded impurities and inorganic residues. The subsequent KOH treatment further enhanced this process by removing stable impurities, such as silicates and carbonates, resulting in the lowest ash content of 7.02% at this concentration. Beyond 6 M, the reduction in ash content plateaued, indicating that further increases in HCl concentration had no impact on the demineralization process.

During the demineralization process, HCl reacted with zinc oxide (ZnO) and $Fe_2O_3$ compounds. ZnO, commonly used as a vulcanization activator,[31] and $Fe_2O_3$,[32] originating from steel belting within tires, contributed to ash content. HCl broke down into hydrogen ions ($H^+$), which reacted with the metal oxides to form zinc chloride ($ZnCl_2$) and iron chloride ($FeCl_2$). These metal chlorides were water soluble and were removed during the washing process. The reactions were represented in Eqs. (4) and (5):[33]

$$ZnO + 2HCl \rightarrow ZnCl_2 + H_2O \quad (4)$$

$$Fe_2O_3 + 6HCl \rightarrow 2FeCl_3 + 3H_2O \quad (5)$$

While HCl efficiently removed metal oxides, stable non-metallic impurities, such as aluminum silicate ($Al_2SiO_5$) and $CaCO_3$, it resisted dissolution due to the stability of its chemical structures.[34,35] $Al_2SiO_5$

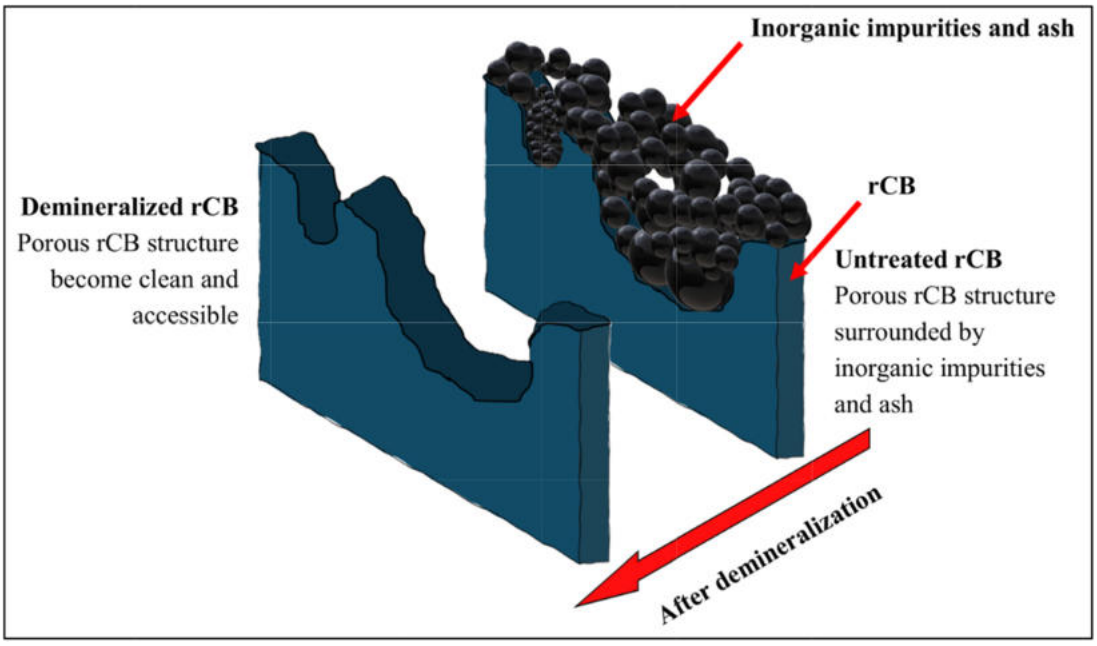


**Fig. 3.** Effect of demineralization on the removal of impurities from the porous structure of rCB.

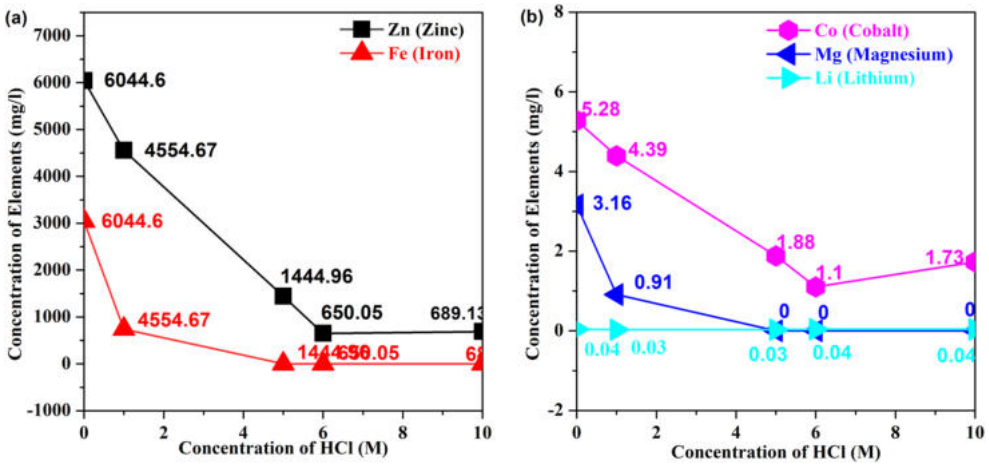


**Fig. 4.** Concentration of metal impurities in rCB after demineralization with varying HCl concentrations followed by 6M KOH at 25°C for 1h.

and $CaCO_3$ were incorporated into tires as reinforcing agents and fillers to enhance mechanical strength, heat resistance, and production efficiency. To remove these impurities, KOH was introduced in the second phase of demineralization. The hydroxide ions ($OH^-$) dissociated from KOH and reacted with $Al_2SiO_5$ and $CaCO_3$ to form soluble potassium silicate ($K_2SiO_3$) and potassium carbonate ($K_2CO_3$), which were removed in subsequent washing steps. These reactions were represented in Eqs. (6) and (7):[33]

$$Al_2SiO_5 + 2KOH \rightarrow 2K_2SiO_3 + Al_2O_3 \quad (6)$$

$$CaCO_3 + 2KOH \rightarrow K_2CO_3 + H_2O \quad (7)$$

The combined acid-base treatment, as illustrated in Fig. 3, effectively removed both metallic and non-metallic impurities from rCB. This process eliminated the inorganic residues and ash, exposed the porous structure, and made it more accessible for further activation treatment.

### *Inductively coupled plasma optical emission spectroscopy (ICP-OES)*

Results of ICP-OES analysis have shown the presence of Zn, Fe, Co, Mg, and Li metals in the raw rCB samples, which contributed to the high ash content. Fig. 4 shows the results for ICP analysis of rCB after demineralization using various HCl

concentrations and 6 M KOH. The Zn concentration decreased from 6044.6 mg $L^{-1}$ to 650.05 mg $L^{-1}$ at 6 M HCl, indicating efficient demineralization. Cardona-Uribe et al.[22] also reported a reduction in ZnO content from 31 wt% to 9.50 wt% with 5 M HCl, while Qiao et al.[36] observed a further decrease from 16.35 wt% to 1.07 wt% using 30 wt% HCl.

This reduction was due to the conversion of ZnO into soluble $ZnCl_2$ as described in Eq. (5). Fe, the second most abundant metal, decreased from 3043.93 mg $L^{-1}$ to 741.44 mg $L^{-1}$ at 1 M HCl and was completely removed at concentrations beyond 5 M HCl. The absence of Fe at higher HCl concentrations was attributed to the high solubility of $FeCl_3$. This finding aligned with previous studies; Cardona-Uribe et al.[22] reported that at 5 M HCl, $Fe_2O_3$ content decreased from 4.00 wt% to 3.32 wt%, while treatment with $HNO_3$ reduced it to 3.70 wt%. Similarly, Qiao et al.[36] reported a reduction in $Fe_2O_3$ content from 1.63 wt% to 0.57 wt% with HCl.

Cobalt (Co) concentration decreased from 5.28 mg $L^{-1}$ to 1.1 mg $L^{-1}$ at 6 M HCl, while magnesium (Mg) was completely removed beyond 1 M HCl. Qiao et al.[36] reported a similar trend, reduction of MgO content from 1.42 wt% to 1.24 wt% following HCl treatment. Lithium (Li) concentrations remained consistently low, ranging from 0.03 to 0.04 mg $L^{-1}$. The results indicated that the removal of Zn and Co reached a plateau at HCl concentrations exceeding 6 M, whereas Fe, Mg, and Li were entirely removed. These findings were supported by ash content analysis, which also exhibited a plateau at higher HCl concentrations.

### *Brunauer–emmett–teller (BET) and surface area and iodine adsorption number (IAN)*

Fig. 5 shows the BET and IAN results for rCB, both of which exhibited a plateau when subjected to different concentrations of HCl. Similar trends were reported by Cardona-Uribe et al.[22] with plateaus ranging from 32 $m^2$ $g^{-1}$ to 39 $m^2$ $g^{-1}$ and 40 $m^2$ $g^{-1}$ when treated with 5 M HCl and 5 M $HNO_3$. Qiao et al.[36] also reported a plateau ranging from 50.02 $m^2$ $g^{-1}$ to 53.72 $m^2$ $g^{-1}$ after treatment with 30 wt% HCl.

Similarly, the total pore volume (VT) in Table 3 exhibited a plateau, ranging from 0.0594 $cm^3$ $g^{-1}$ for D0 to 0.0941 $cm^3$ $g^{-1}$ for D10, aligned with the reported plateau of 0.078 $cm^3$ $g^{-1}$ to 0.293 $cm^3$ $g^{-1}$ [22] observed with HCl treatment. Furthermore, low micropore area ($S_{mi}$) of less than 3.5 $m^2$ $g^{-1}$ further supported the observation that demineralization did not enhance surface area or porosity of rCB.

Fig. 6a shows the adsorption-desorption isotherms of rCB. The plateau hysteresis loop exhibited an

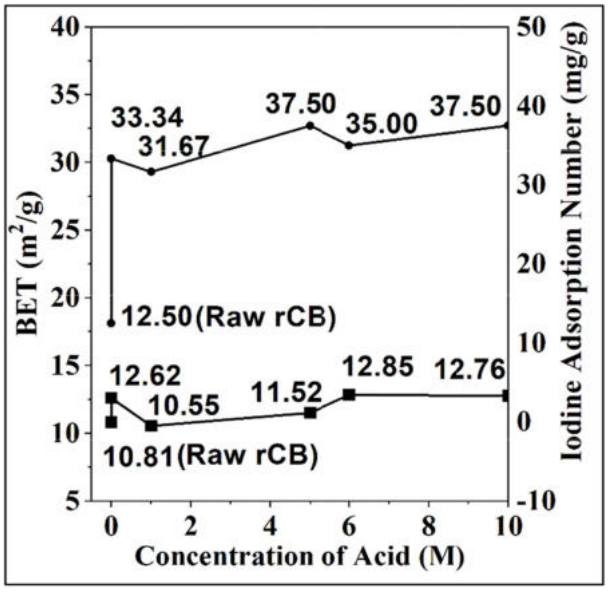


**Fig. 5.** BET surface area and iodine adsorption number of rCB after demineralization with varying HCl concentrations, followed by 6M KOH at 25°C for 1h.

H3 pattern, indicating the presence of mesoporous structures with slit-shaped pores formed by plate-like particle aggregates.[15,37] Meanwhile, Fig. 6b shows the pore-size distribution of rCB, with a plateau in the mesopore range. Qiao et al.[36] reported that the majority of pores in rCB were concentrated within a size range of 10–100 nm.

### *Cost evaluation*

A cost evaluation of the demineralized rCB was conducted to determine the optimum concentration of HCl that enhances the performance of rCB. A comparison of the treatment costs using 5 M and 6 M HCl was conducted based on the yield, ash content, and BET surface area of rCB. Table 4 shows the cost evaluation and performance comparison of rCB treated with 5 M and 6 M HCl.

The analysis showed that 5 M HCl was more cost-effective than 6 M HCl, reducing costs by 20%. While 6 M HCl demonstrated slightly better performance with a 1.12% increase in yield (from 91.95% to 92.98%), a 7.37% reduction in ash content (from 42.34% to 49.71%), and a 12.33% improvement in BET surface area (from 6.48 % to 18.80 %), these improvements are insufficient to justify the 20% increased cost. Therefore, 5 M HCl was selected as the optimal concentration, offering a balance between cost-effectiveness and optimum performance. Consequently, the D5 sample was chosen for further physical activation treatments.

**Table 3.** BET surface area, micropore area, total pore volume, micropore volume, and pore diameter of raw and demineralized rCB with varying HCl concentrations followed by 6M KOH at 25°C for oneh.

| Sample | $S_{BET}$ ($m^2$ $g^{-1}$) | $S_{mi}$ ($m^2$ $g^{-1}$) | $V_T$ ($cm^3$ $g^{-1}$) | $V_{mi}$ ($cm^3$ $g^{-1}$) | $D_P$ adsorption (nm) |
|---|---|---|---|---|---|
| Raw rCB | 10.81 | 2.77 | 0.0715 | 0.0000 | 40.98 |
| D0 | 12.62 | 2.98 | 0.0594 | 0.0000 | 29.40 |
| D1 | 10.55 | 3.14 | 0.0883 | 0.0002 | 53.87 |
| D5 | 11.51 | 3.33 | 0.0682 | 0.0001 | 43.77 |
| D6 | 12.85 | 3.45 | 0.0867 | 0.0000 | 43.93 |
| D10 | 12.76 | 3.35 | 0.0941 | 0.0000 | 48.19 |

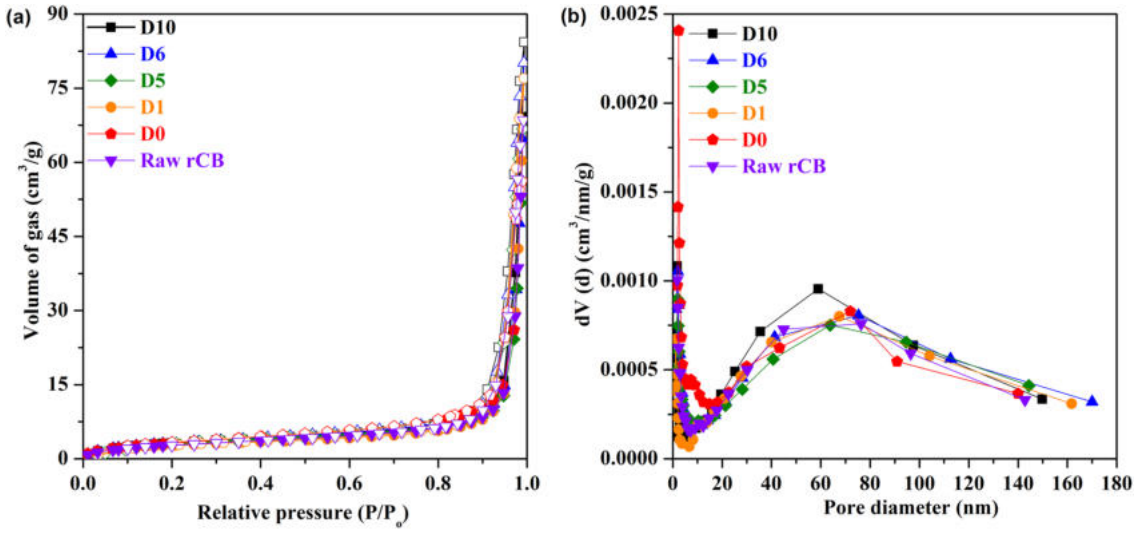


**Fig. 6.** (a) Adsorption-desorption hysteresis loop (b) Pore size distribution of rCB after demineralization with varying HCl concentrations followed by 6M KOH at 25°C for 1h.

**Table 4.** Cost evaluation and performance comparison of rCB treated with 5 M and 6 M HCl followed by 6M KOH at 25°C for 1h.

| Parameter | 5 M HCl | 6 M HCl | Difference (%) |
|---|---|---|---|
| Cost (RM) | 323.23 | 388.13 | + 20.08 |
| Yield (%) | 91.95 | 92.98 | + 1.12 |
| Ash (%) | 42.34 | 49.71 | – 7.37 |
| BET surface area ($m^2$ $g^{-1}$) | 6.48 | 18.80 | + 12.33 |
| IAN (mg $g^{-1}$) | 12.48 | 4.98 | – 7.5 |

## *Physical activation of demineralized rCB*

### *Brunauer–emmett–teller (BET)*

Fig. 7a, 7b, and 7c show the BET surface area, micropore surface area ($S_{mic}$), and total pore volume ($V_T$), respectively, of rCB subjected to physical activation at different temperatures and durations.

The BET surface area, $S_{mic}$, and $V_T$ exhibited an increasing trend with rising activation temperatures, followed by a sharp decline at 500°C. BET surface area increased from 39.17 $m^2$ $g^{-1}$ at 300°C to 114.41 $m^2$ $g^{-1}$ at 350°C and reached a maximum of 188.52 $m^2$ $g^{-1}$ at 450°C for 2 h. Similarly, $S_{mic}$ increased from 22.86 $m^2$ $g^{-1}$ at 300°C to 65.09 $m^2$ $g^{-1}$ at 400°C, attaining its maximum value of 84.22 $m^2$ $g^{-1}$ at 450°C for 2 h. This trend was further supported by $V_T$, which increased from 0.1008 $cm^3$ $g^{-1}$ at 300°C to 0.3548 $cm^3$ $g^{-1}$ at 400°C, peaking at 0.3891 $cm^3$ $g^{-1}$ at 450°C for 1 h.

The increases in BET surface area, $S_{mic}$, and $V_T$ were attributed to the thermal cracking of carbonaceous materials and the removal of volatile compounds, which promoted the formation and development of new pores.[37] However, at 500°C, the BET surface area decreased sharply for all activation durations, with a corresponding reduction in total pore volume. These declines were caused by severe thermal degradation, including pore collapse and sintering, which led to structural densification and reduced porosity.[33,38]

These findings demonstrated that 450°C for 2 h was the optimal activation condition, as it achieved the highest BET surface area, micropore surface area, and total pore volume while avoiding excessive thermal damage. Fig. 8 illustrates the evolution of pore structures in rCB with increasing temperature. At 300°C, the initial development of micropores and mesopores occurred as thermal cracking began to remove volatile compounds.[37] As the temperature increased to 450°C, the formation of well-balanced mesoporous and microporous structures was maximized, achieving the highest BET surface area, micropore surface

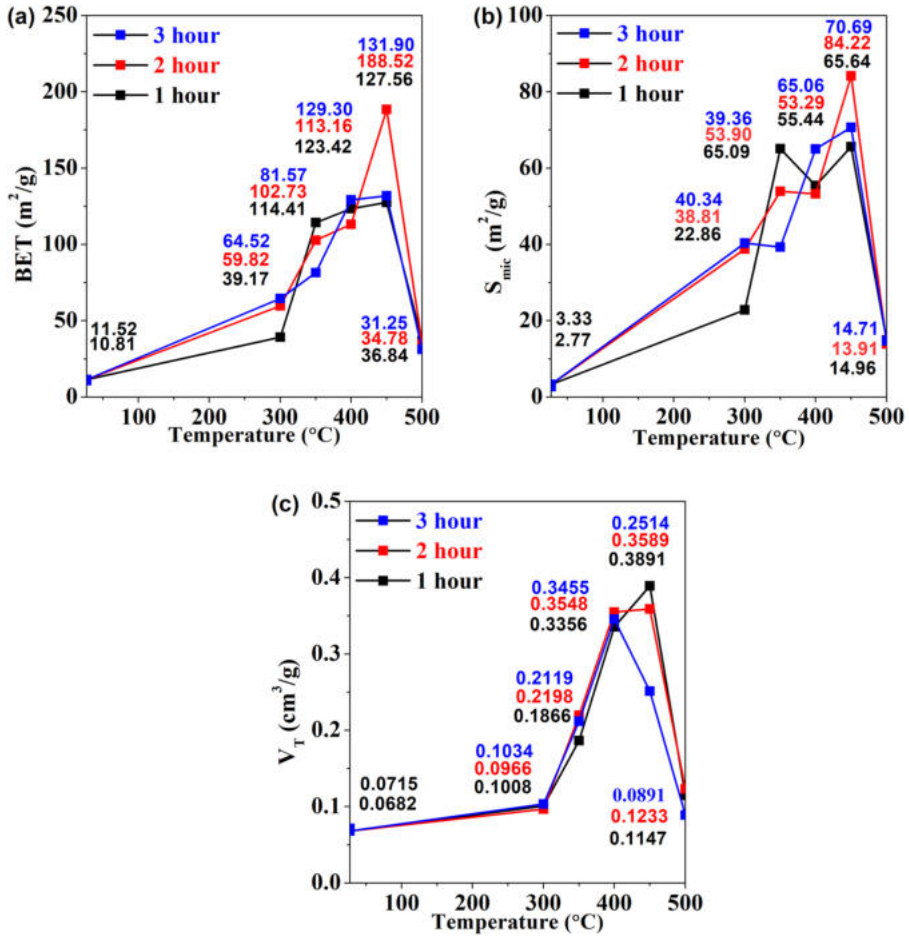


**Fig. 7.** (a) Total BET surface area, (b) micropore surface area (Smic), and (c) total volume ($V_T$) of rCB activated at 300–500°C for 1–3h.

area, and total pore volume. However, at 500°C, severe thermal degradation led to pore merging, collapse, and sintering, resulting in a 33% reduction in porosity. This visual representation reinforced the observed trends and highlighted the critical balance between temperature and structural integrity in determining the optimal activation conditions.

The burn-off percentage increased with both temperature and duration, aligning with the trends observed in BET surface area (Table 5). At 300°C, the low burn-off percentage (16.66–20.65%) corresponds to minimal increases in surface area due to controlled volatile removal. Between 350°C and 400°C, burn-off values rose (39.39–75.31%), leading to substantial increases in surface area, which peaked at 450°C (188.52 $m^2$ $g^{-1}$). However, at 500°C, excessive burn-off (94.25–96.30%) resulted in pore collapse and structural degradation, causing sharp declines in surface area. These findings underscore the importance of achieving a balanced activation condition to maximize porosity while avoiding excessive thermal damage.

Fig. 9 shows the nitrogen adsorption-desorption isotherms for rCB activated at various temperatures and durations. The nitrogen adsorption-desorption isotherms showed the effect of activation duration (1, 2, and 3 h) on gas adsorption. At 1 h, the volume of gas adsorbed continued to increase with increasing temperatures, reaching a peak of 316.87 $cm^3$ $g^{-1}$ at 450°C (D5/AC450-1). A well-defined H3-type hysteresis loop, indicative of slit-shaped mesopores,[7] was observed, reflecting optimal pore development due to thermal cracking and volatile removal. The phases of adsorption and pore filling during the isotherm process were illustrated in Fig. 10, which depicted the sequential adsorption mechanism.

Fig. 10 shows the mechanism of the adsorption and desorption process. In the adsorption phase, gas molecules were initially adsorbed onto the rCB surface. As pressure increased, gas molecules uniformly covered the surface, forming the monolayer phase. Further increases in pressure led to the multilayer phase, wherein smaller pores were filled as gas molecules formed multiple layers. Finally, during the

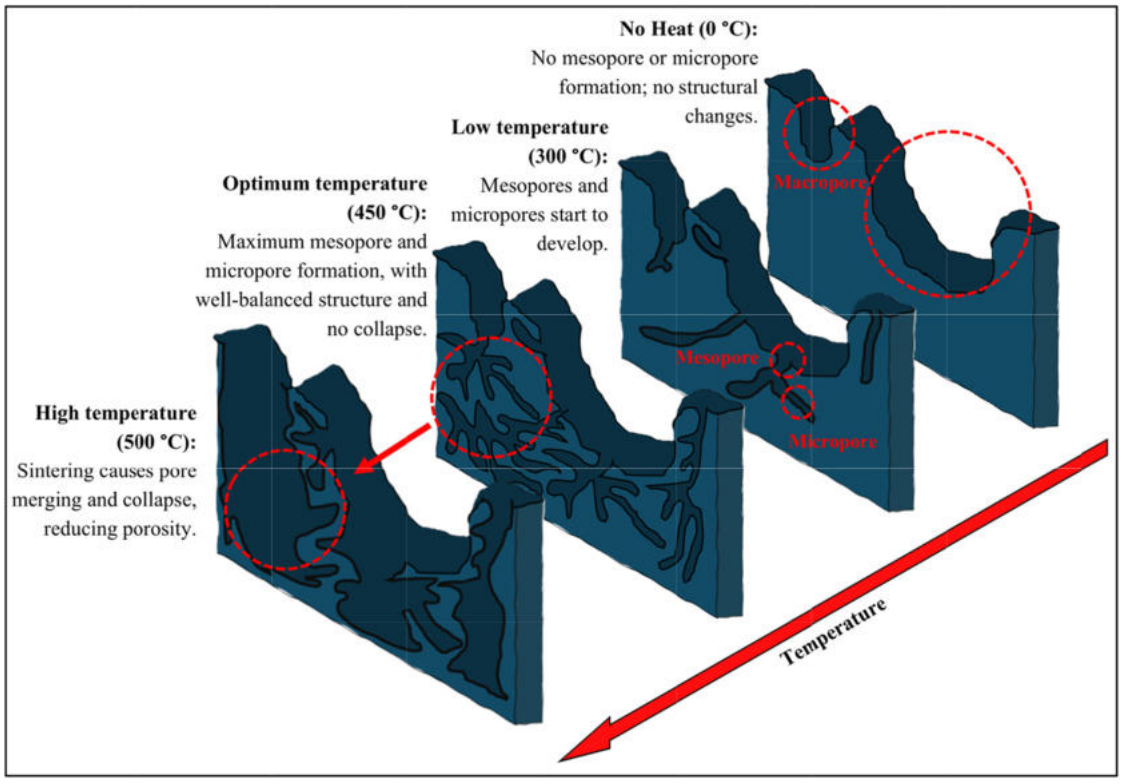


**Fig. 8.** Effect of temperature on the porosity structure of rCB.

**Table 5.** BET surface area, micropore area, total volume, volume of micropore, pore diameter, adsorption, and desorption of rCB activated at 300–500°C for 1–3h.

| Sample | $S_{BET}$ ($m^2$ $g^{-1}$) | $S_{mic}$ ($m^2$ $g^{-1}$) | $V_T$ ($cm^3$ $g^{-1}$) | $V_{mi}$ ($cm^3$ $g^{-1}$) | $D_P$ adsorption (nm) | Burn–off (%) |
|---|---|---|---|---|---|---|
| Raw rCB | 10.81 | 2.77 | 0.0715 | 0.0000 | 40.98 | – |
| D5 | 11.52 | 3.33 | 0.0682 | 0.0001 | 43.77 | – |
| D5/AC300-1 | 39.17 | 22.86 | 0.1008 | 0.0079 | 18.06 | 16.66 |
| D5/AC300-2 | 59.82 | 38.81 | 0.0966 | 0.0143 | 14.61 | 20.65 |
| D5/AC300-3 | 64.52 | 40.34 | 0.1034 | 0.0145 | 13.70 | 20.21 |
| D5/AC350-1 | 114.41 | 65.09 | 0.1866 | 0.0228 | 12.05 | 39.39 |
| D5/AC350-2 | 102.73 | 53.90 | 0.2198 | 0.0197 | 14.56 | 46.43 |
| D5/AC350-3 | 81.57 | 39.36 | 0.2119 | 0.0138 | 15.86 | 50.00 |
| D5/AC400-1 | 123.42 | 55.44 | 0.3356 | 0.0190 | 17.49 | 63.33 |
| D5/AC400-2 | 113.16 | 53.29 | 0.3548 | 0.0188 | 20.52 | 71.35 |
| D5/AC400-3 | 129.30 | 65.06 | 0.3455 | 0.0227 | 18.39 | 75.31 |
| D5/AC450-1 | 127.56 | 65.64 | 0.3891 | 0.0222 | 21.64 | 77.26 |
| D5/AC450-2 | 188.52 | 84.22 | 0.3589 | 0.0276 | 17.07 | 82.87 |
| D5/AC450-3 | 131.90 | 70.69 | 0.2514 | 0.0244 | 15.25 | 88.48 |
| D5/AC500-1 | 36.84 | 14.96 | 0.1147 | 0.0046 | 19.11 | 94.25 |
| D5/AC500-2 | 34.78 | 13.91 | 0.1233 | 0.0042 | 20.46 | 95.75 |
| D5/AC500-3 | 31.25 | 14.71 | 0.0891 | 0.0049 | 19.66 | 96.30 |

condensation phase, higher relative pressure resulted in the complete filling of mesopores,[39] as depicted by the hysteresis loop, which enabled the calculation of pore size, volume, and distribution using the Barrett-Joyner-Halenda (BJH) method.

Extending the duration to 2 h further enhanced gas adsorption, reaching 331.78 $cm^3$ $g^{-1}$ at 450°C (D5/AC450-2). The hysteresis loop became more distinct, indicating improved mesopore connectivity and the development of well-structured pores. The longer duration facilitated more thorough volatile removal and promoted the formation of interconnected mesopores and micropores.

However, at 3 h, gas adsorption capacity decreased across all temperatures. This reduction is attributed to structural degradation at increasing temperatures, where prolonged thermal exposure caused pore wall thinning, coalescence, and eventual

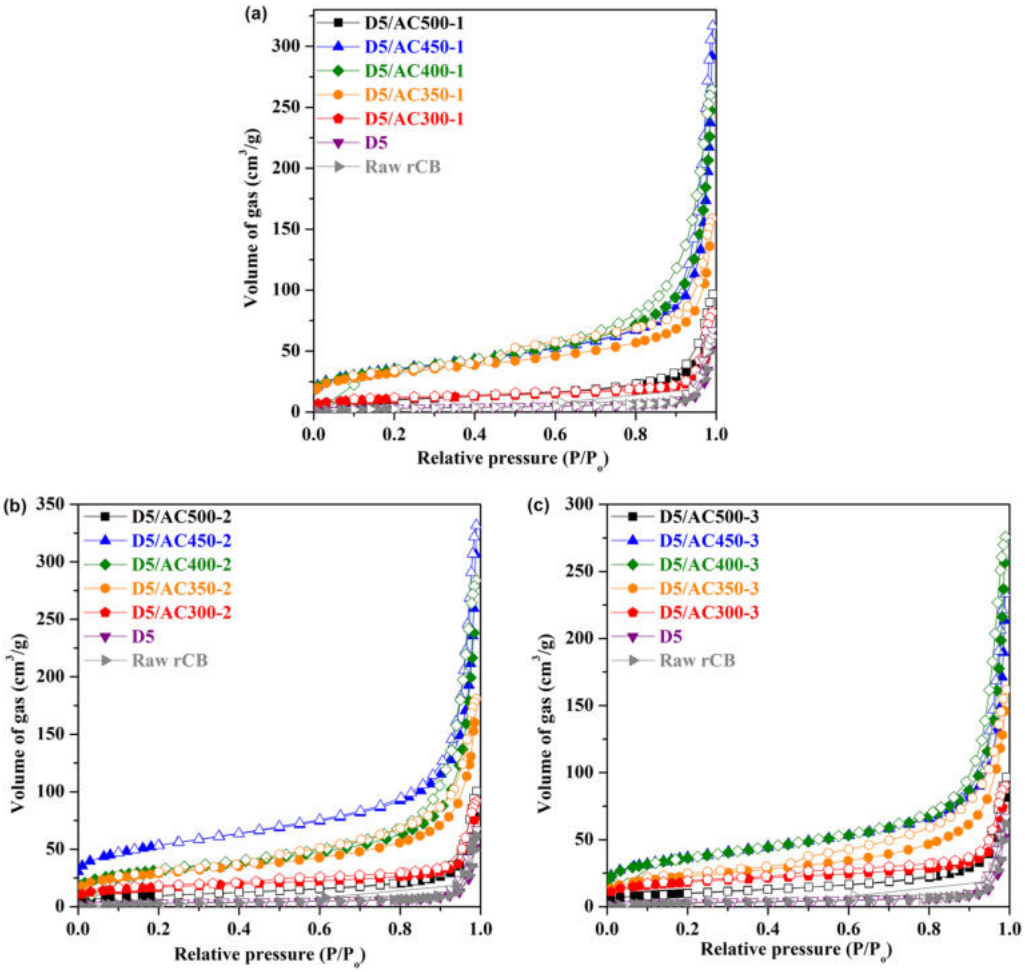


**Fig. 9.** Adsorption-desorption hysteresis loop of rCB activated at 300–500°C for 1–3h: (a) 1 h, (b) 2h, (c) 3h.

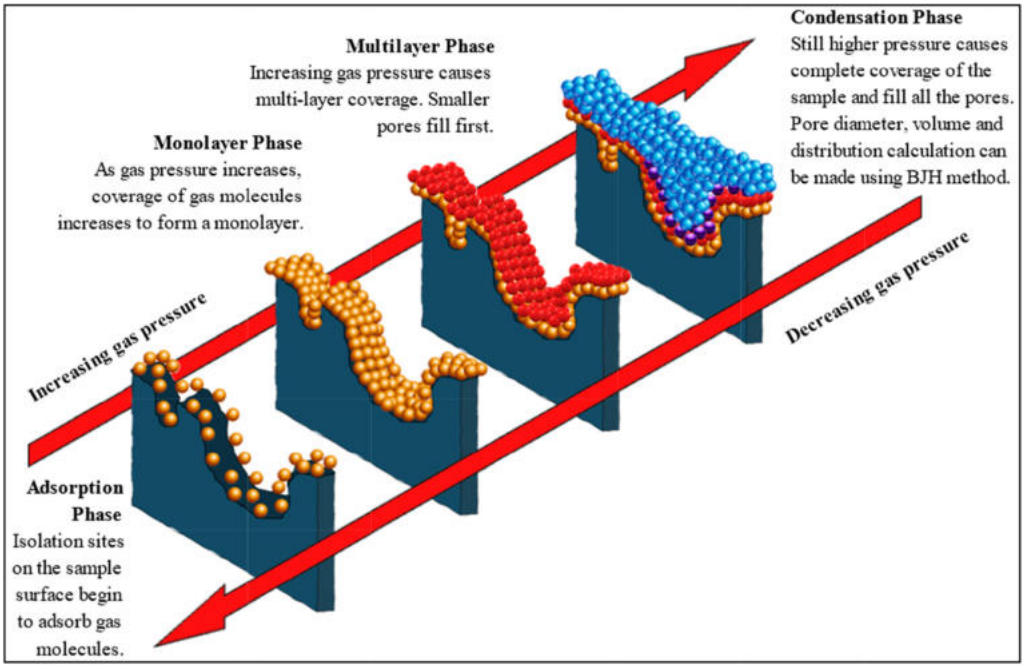


**Fig. 10.** Mechanism of the nitrogen adsorption-desorption process on the surface structure of rCB, illustrating the adsorption, monolayer, multilayer, and condensation phases.

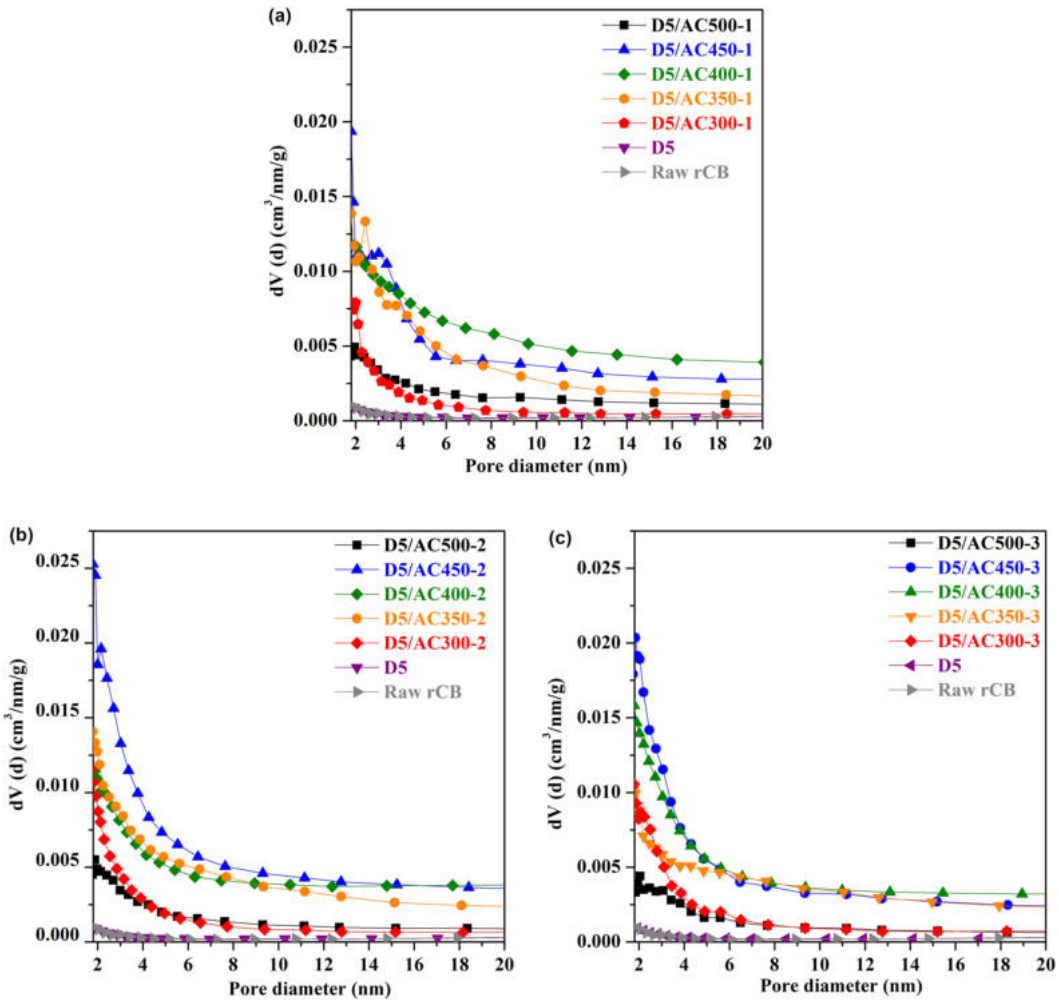


**Fig. 11.** Pore size distribution of rCB activated at 300–500°C for 1–3h: (a) 1 h, (b) 2 h, (c) 3 h.

collapse of microporous structures, thereby reducing available surface area and porosity. This interpretation is supported by the reduction of BET surface area from 188.52 to 31.25$m^2g^{-1}$, micropore surface area from 84.22 to 14.71$m^2g^{-1}$, total pore volume from 0.3891 to 0.0891$cm^3g^{-1}$, iodine number from 100.01 to 11.25$mgg^{-1}$ and extreme burn-off of 96.30 % in rCB treated at 500°C. A similar trend was reported by Li et al.,[40] where BET surface area decreased from 789.63 to 459.43$m^2g^{-1}$ and the total pore volume reduced from 0.4531 to 0.2755$cm^3g^{-1}$ after activation at 850°C for 90min.

Fig. 11 shows the pore size distribution (PSD) of rCB activated at various temperatures and durations.

The PSD at 450°C for 2 h demonstrated the most effective micropore development, with the highest micropore volume of 0.02528 $cm^3$ $nm^{-1}$ $g^{-1}$. This condition balanced thermal energy and activation duration, enabling efficient volatile removal and improved pore connectivity.[33] In comparison, 450°C for 1 h resulted in a lower micropore volume of 0.01937 $cm^3$ nm-1 g-1, as the shorter activation time limited pore formation. Extending the duration to 3 h reduced the micropore volume to 0.01793 $cm^3$ $nm^{-1}$ $g^{-1}$, due to pore coalescence and collapse caused by prolonged thermal exposure.

At 300°C and 350°C, insufficient thermal energy hindered the development of both micropores and mesopores, resulting in minimal pore volumes. At 500°C, excessive thermal energy resulted in severe structural degradation and densification, leading to reductions in pore volume across all activation durations. These findings emphasized 450°C for 2 h as the optimal activation condition, achieving the best balance between effective pore development and structural preservation.

### *Iodine adsorption number (IAN)*

Fig. 12 shows the IAN results for rCB for rCB activated at various temperatures and durations.

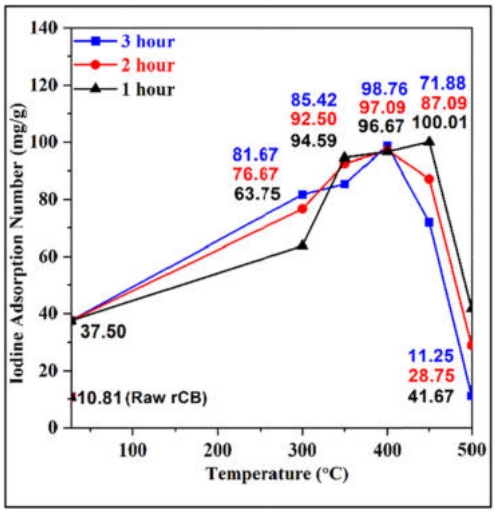


**Fig. 12.** Iodine adsorption number of rCB activated at 300–500°C for 1–3h.

The IAN results showed that 450°C for 1 h achieved the highest adsorption capacity of 100.01 mg $g^{-1}$, indicating optimal activation conditions for iodine adsorption in liquid-phase applications. For 2 h and 3 h at 450°C, the IAN values decreased to 87.09 mg $g^{-1}$ and 71.88 mg $g^{-1}$, respectively, suggesting that 1 h provided the ideal duration for maximizing adsorption performance without causing structural degradation. At 300°C and 350°C, the IAN increased progressively, reaching 92.50 mg $g^{-1}$ at 350°C for 2 h but remained below the optimal performance observed at 450°C. Taufany et al.[41] reported that activation at 300°C for 1 h achieved the highest IAN of 293.3 mg $g^{-1}$, which decreased to 259 mg $g^{-1}$ with increasing activation duration, emphasizing the impact of temperature and time on iodine adsorption efficiency. At 500°C, the IAN dropped sharply across all durations, with the lowest value of 11.25 mg $g^{-1}$ at 3 h, reflecting severe structural degradation and pore collapse. These findings emphasized that 450°C for 1 h is the most effective activation condition for iodine adsorption, striking a balance between optimal pore development and structural integrity.

## Conclusion

This study investigated the combined effects of demineralization and physical activation on the porous structure, surface area, and adsorption properties of rCB to enhance its applicability in adsorption processes. The findings emphasized the complementary roles of these treatments in improving the physicochemical properties of rCB. The demineralization of rCB with 5 M HCl was identified as the optimal treatment, reducing costs by 20% compared to 6 M HCl while maintaining effective performance. This treatment reduced the ash content to 8.05%, removed impurities such as Zn and Fe, and exposed functional groups (including-OH, C=O, and C-O), thereby enhancing surface reactivity. However, the BET surface area (12.85 $m^2$ $g^{-1}$) and iodine adsorption capacity (37.5 mg $g^{-1}$) plateaued, indicating that demineralization was only effective in removing the inorganic impurities and did not enhance the surface area or porosity of rCB. Conversely, physical activation enhanced the surface area and porosity of demineralized rCB. Activation at 450°C for 2 h yielded the highest BET surface area (188.52 $m^2$ $g^{-1}$) and total pore volume (0.3589 $cm^3$ $g^{-1}$), indicating the formation of a well-developed porous structure with interconnected mesopores and micropores suitable for gas-phase adsorption. For liquid-phase applications, activation at 450°C for 1 h achieved the highest iodine adsorption number (IAN) of 100.01 mg $g^{-1}$. However, at 500°C, excessive thermal degradation caused pore coalescence, structural collapse, and reduced surface area and porosity. Demineralization improved the chemical purity and surface functionality of rCB, while physical activation at 450°C for 1–2 h, achieved high surface area and porosity. The synergistic application of these treatments provided an effective strategy for producing high-performance rCB adsorbents suitable for removing dyes and heavy metals from aqueous and gaseous environments.

## Acknowledgement

The authors gratefully acknowledge the Advanced Materials and Polymers Laboratory and the Faculty of Applied Sciences at Universiti Teknologi MARA for providing the necessary facilities and technical support.

## Authors' declaration

- Conflicts of Interest: None.
- We confirm that all Figures and Tables presented in this manuscript are ours. Any Figures or images not created by us have been incorporated with the appropriate permissions for re-publication, which are duly attached to the manuscript.
- No animal studies are presented in the manuscript.
- No human studies are presented in the manuscript.
- Ethical Clearance: The project was approved by the local ethical committee at Universiti Teknologi Mara.

## Authors' contribution statement

S.N.R.M.Z., N.F.A.Z., and C.C.T. conceptualized and designed the study. S.N.R.M.Z. acquired the data, performed the experimental work, carried out analysis and interpretation, and drafted the manuscript. N.F.A.Z. and C.C.T. contributed to data interpretation. H.A.R. and S.I.A.H. revised and proofread the manuscript. All authors reviewed and approved the final version of the manuscript.

## Funding statement

This research was financially supported by the Ministry of Higher Education Malaysia under the Fundamental Research Grant Scheme (Grant No. FRGS/1/2024/STG05/UITM/02/24).

## Supplementary materials

Supplementary materials is available at https://doi.org/10.21123/2411-7986.-19.

## References

1. Mouneir SM, El-Shamy AM. A review on harnessing the energy potential of pyrolysis gas from scrap tires: Challenges and opportunities for sustainable energy recovery. J Anal Appl Pyrolysis. 2024;177(December 2023):106302. https://doi.org/10.1016/j.jaap.2023.106302.
2. Abdulfattah O, Abdalla R. Addressing the Issue of Microparticle Size Pyrolysis Carbon Black (PCB) by Adding to the Concrete Mixture. An-Najah Univ J Res – A Nat Sci. 2024;38(2):107–111. https://doi.org/10.35552/anujr.a.38.2.2205.
3. Ghode P, Bhosale S, Survase R, Sarwade P, Dahake AG. USE OF WASTE RUBBER TYRE IN CONSTRUCTION OF BITUMINOUS ROAD. Int Res J Mod Eng Technol Sci. 2023;00(08):1395–1397. https://doi.org/10.56726/irjmets44098.
4. Gefenienė A, Zubrytė E, Kaušpėdienė D, Ramanauskas R, Ragauskas R. Firefighting Wastewater from a Tire Recycling Plant: Chemical Characterization and Simultaneous Removal of Multiple Pollutants. 2023;6(6):1–4. http://dx.doi.org/10.2139/ssrn.4631687.
5. Jiang Y, Wang C, Ma L, Gao T, Wāng Y. Environmental profiles, hazard identification, and toxicological hallmarks of emerging tire rubber-related contaminants 6PPD and 6PPD-quinone. Environ Int. 2024;187(April). https://doi.org/10.1016/j.envint.2024.108677.
6. Lane RF, Smalling KL, Bradley PM, *et al.* Tire-derived contaminants 6PPD and 6PPD-Q: Analysis, sample handling, and reconnaissance of United States stream exposures. Chemosphere. 2024;363(July):142830. https://doi.org/10.1016/j.chemosphere.2024.142830.
7. Ali UFM, Hussin F, Gopinath SCB, *et al.* Advancement in recycling waste tire activated carbon to potential adsorbents. Environ Eng Res. 2022;27(6):0–1. https://doi.org/10.4491/eer.2021.452.
8. Singh B, Kaunert C, Malviya R. Featuring machine learning in municipal solid waste management: Technological advancements in waste sorting and processing ropeway for SDG 13 (climate action). In: Municipal Solid Waste Management and Recycling Technologies. 2024:343–366. https://doi.org/10.4018/979-8-3693-4054-7.ch013.
9. Halkos GE, Aslanidis PSC. Reviewing the integrated institutional waste-related framework for circular economy in the European Union. Waste Manag Bull. 2024;2(3):28–35. https://doi.org/10.1016/j.wmb.2024.06.002.
10. Urrego-Yepes W, Cardona-Uribe N, Vargas-Isaza CA, Martínez JD. Incorporating the recovered carbon black produced in an industrial-scale waste tire pyrolysis plant into a natural rubber formulation. J Environ Manage. 2021;287(February). https://doi.org/10.1016/j.jenvman.2021.112292.
11. Bowles AJ, Wilson AL, Fowler GD. Synergistic benefits of recovered carbon black demineralisation for tyre recycling. Resour Conserv Recycl. 2023;198(July):107124. https://doi.org/10.1016/j.resconrec.2023.107124.
12. Kassahun E, Mekuria S, Beyan SM. Specific Surface Area Enhancement of Waste Tire-Based Activated Carbon by Demineralization Technique and Adsorption of Methylene Blue. Int J Chem Eng. 2022;2022. https://doi.org/10.1155/2022/8198551.
13. Hou SP, Zhang D, Xie ZP, *et al.* Activated carbon prepared from waste tire pyrolysis carbon black via CO2/KOH activation used as supercapacitor electrode. Sci China Technol Sci. 2022;65(10):2337–2347. https://doi.org/10.1007/s11431-021-2032-3.
14. Dziejarski B, Hernández-Barreto DF, Moreno-Piraján JC, *et al.* Upgrading recovered carbon black (rCB) from industrial-scale end-of-life tires (ELTs) pyrolysis to activated carbons: Material characterization and CO2 capture abilities. Environ Res. 2024;247(18). https://doi.org/10.1016/j.envres.2024.118169.
15. Alqadami AA, Wabaidur SM, Jeon BH, Khan MA. Co-hydrothermal valorization of food waste: process optimization, characterization, and water decolorization application. Biomass Convers Biorefinery. 2024;14(14):15757–15768. https://doi.org/10.1007/s13399-022-03711-7.
16. Azam M, Wabaidur SM, Khan MR, Al-Resayes SI, Islam MS. Heavy Metal Ions Removal from Aqueous Solutions by Treated Ajwa Date Pits: Kinetic, Isotherm, and Thermodynamic Approach. Polymers (Basel). 2022;14(5). https://doi.org/10.3390/polym14050914.
17. Sivasankarapillai VS, Baskaran S, Sundararajan A, *et al.* Porous network of nitrogen self-doped honeycomb like activated carbon derived from Caladium tricolor leaves: a multifunctional platform for energy and environmental applications. J Porous Mater. 2024;31(4):1489–1502. https://doi.org/10.1007/s10934-024-01580-1.
18. Ali I, Alharbi OML, ALOthman ZA, Alwarthan A, Al-Mohaimeed AM. Preparation of a carboxymethylcellulose-iron composite for uptake of atorvastatin in water. Int J Biol Macromol. 2019;132:244–253. https://doi.org/10.1016/j.ijbiomac.2019.03.211.
19. Costa SMR, Fowler D, Carreira GA, Portugal I, Silva CM. Production and Upgrading of Recovered Carbon Black from the Pyrolysis of End-of-Life Tires. Materials (Basel). 2022;15(6). https://doi.org/10.3390/ma15062030.
20. Martínez JD, Cardona-Uribe N, Murillo R, García T, López JM. Carbon black recovery from waste tire pyrolysis by demineralization: Production and application in rubber compounding. Waste Manag. 2019;85:574–584. https://doi.org/10.1016/j.wasman.2019.01.016.

21. Cardona-Uribe N, Betancur M, Martínez JD. Towards the chemical upgrading of the recovered carbon black derived from pyrolysis of end-of-life tires. Sustain Mater Technol. 2021;28. https://doi.org/10.1016/j.susmat.2021.e00287.
22. Evans TG, Salinger JL, Bingel LW, Walton KS. Determining Surface Areas and Pore Volumes of Metal-Organic Frameworks. J Vis Exp. 2024;2024(205):1–12. https://doi.org/10.3791/65716.
23. Tian X, Zhuang Q, Han S, *et al.* A novel approach of reapplication of carbon black recovered from waste tyre pyrolysis to rubber composites. J Clean Prod. 2021;280:124460. https://doi.org/10.1016/j.jclepro.2020.124460.
24. Kusi DA, Arthur EK, Gikunoo E, *et al.* Electrochemical performance of chemically treated pyrolytic carbon black from waste car tyres. Energy Nexus. 2024;14(March):100297. https://doi.org/10.1016/j.nexus.2024.100297.
25. Tsipa PC, Phiri MM, Iwarere SA, Mkhize NM, Phiri MJ, Hlangothi SP. A novel chemical pre-pyrolysis treatment of waste tyre crumbs: A viable way for low temperature waste tyre pyrolysis. J Anal Appl Pyrolysis. 2024;181(June):106631. https://doi.org/10.1016/j.jaap.2024.106631.
26. González-González RB, González LT, Iglesias-González S, *et al.* Characterization of chemically activated pyrolytic carbon black derived from waste tires as a candidate for nanomaterial precursor. Nanomaterials. 2020;10(11):1–22. https://doi.org/10.3390/nano10112213.
27. Kareem MM, Kadem BY, Mohammad EJ, Atiyah AJ. Synthesis, characterization and gas sensor application of new composite based on MWCNTs:CoPc:Metal oxide. Baghdad Sci J. 2021;18(2):384–392. https://doi.org/10.21123/BSJ.2021.18.2.0384.
28. Qiu C, Jiang L, Gao Y, Sheng L. Materials & Design Effects of oxygen-containing functional groups on carbon materials in supercapacitors: A review. Mater Des. 2023;230:111952. https://doi.org/10.1016/j.matdes.2023.111952.
29. Mittal A, Naushad M, Sharma G, Alothman ZA, Wabaidur SM, Alam M. Fabrication of MWCNTs/ThO2 nanocomposite and its adsorption behavior for the removal of Pb(II) metal from aqueous medium. Desalin Water Treat. 2016;57(46):21863–21869. https://doi.org/10.1080/19443994.2015.1125805.
30. Song X, Liu H, Cheng L, Qu Y. Surface modification of coconut-based activated carbon by liquid-phase oxidation and its effects on lead ion adsorption. Desalination. 2010;255(1–3):78–83. https://doi.org/10.1016/j.desal.2010.01.011.
31. Li S, Tran TQ, Li Q, Ji B, Brand AS, Zhang W. Zn leaching recovery and mechanisms from end-of-life tire rubber. Resour Conserv Recycl. 2023;194(March). https://doi.org/10.1016/j.resconrec.2023.107004.
32. Jiang H, Zhang J, Shao J, *et al.* Desulfurization and upgrade of pyrolytic oil and gas during waste tires pyrolysis: The role of metal oxides. Waste Manag. 2024;182:44–54. https://doi.org/10.1016/j.wasman.2024.04.020.
33. Doja S, Pillari LK, Bichler L. Processing and activation of tire-derived char: A review. Renew Sustain Energy Rev. 2022;155. https://doi.org/10.1016/j.rser.2021.111860.
34. Tsitsishvili V, Panayotova M, Mirdzveli N, *et al.* Acid Resistance and Ion-Exchange Capacity of Natural Mixtures of Heulandite and Chabazite. Minerals. 2023;13(3). https://doi.org/10.3390/min13030364.
35. Niu YQ, Liu JH, Aymonier C, *et al.* Calcium carbonate: controlled synthesis, surface functionalization, and nanostructured materials. Chem Soc Rev. 2022;51(18):7883–7943. https://doi.org/10.1039/d1cs00519g.
36. Qiao Y, Chen Z, Wu X, Li Z. Effect of demineralization on waste tire pyrolysis char physical, chemical characteristics and combustion characteristics. Energy. 2023;284(September):129219. https://doi.org/10.1016/j.energy.2023.129219.
37. Doja S, Pillari LK, Bichler L. Processing and activation of tire-derived char: A review. Renew Sustain Energy Rev. 2021;null:null. https://doi.org/10.1016/j.rser.2021.111860.
38. Zerin NH, Rasul MG, Jahirul MI, Sayem ASM. End-of-life tyre conversion to energy: A review on pyrolysis and activated carbon production processes and their challenges. Sci Total Environ. 2023;905(August):166981. https://doi.org/10.1016/j.scitotenv.2023.166981.
39. Kondor A, Santmarti A, Mautner A, Williams D, Bismarck A, Lee KY. On the BET Surface Area of Nanocellulose Determined Using Volumetric, Gravimetric and Chromatographic Adsorption Methods. Front Chem Eng. 2021;3(September):1–12. https://doi.org/10.3389/fceng.2021.738995.
40. Li J, Zhou W, Li J, *et al.* Efficient production of activated carbon with well-developed pore structure based on fast pyrolysis-physical activation. J Energy Inst. 2024;115(May):101685. https://doi.org/10.1016/j.joei.2024.101685.
41. Taufany F, Pasaribu MJ, Romaji BYS, *et al.* The Synthesis of Activated Carbon from Waste Tyre as Fuel Cell Catalyst Support. Evergreen. 2022;9(2):412–420. https://doi.org/10.5109/4794166.

# تأثير إزالة المعادن والتنشيط الفيزيائي في تعزيز المسامية وخصائص الامتزاز للكربون الأسود المستعاد والمحلل حرارياً من الإطارات المستعملة

**سيتي نوراميره ربّاني محمد زاكي[1]، نورول فتاحة أشقين زينال[3،2]، هارتيني أحمد رفائي[2]، سهيلا إدايو عبد الحليم[5،3]، تشيا تشاي تاي[4،3،1]**

[1]كلية العلوم التطبيقية، جامعة التكنولوجيا مارا*(UiTM)* ، فرع سيلانغور، حرم شاه علم، سيلانغور، ماليزيا.
[2]مركز الدراسات التمهيدية، جامعة التكنولوجيا مارا*(UiTM)* ، فرع سيلانغور، حرم دنقل، سيلانغور، ماليزيا.
[3]مجموعة أبحاث تصميم وتصنيع المواد المستدامة*(RIG)* ، جامعة التكنولوجيا مارا*(UiTM)* ، سيلانغور، ماليزيا.
[4]*myBioREC* ، كلية الهندسة المدنية، كلية الهندسة، جامعة التكنولوجيا مارا*(UiTM)* ، سيلانغور، ماليزيا.
[5]شركة إيكو باور سينرجي المحدودة*(Sdn. Bhd.)* ، بندر بوتشونغ جايا، سيلانغور، ماليزيا.

## الملخص

يهدف هذا البحث إلى تحسين البنية المسامية وخصائص الامتزاز للكربون الأسود المستعاد (rCB) من خلال تقنيات إزالة المعادن والتنشيط الفيزيائي. استُخدم حمض الهيدروكلوريك (HCl) بتركيزات مختلفة (1، 5، 6، و10 مول/لتر) لعملية إزالة المعادن، تلتها إضافة هيدروكسيد البوتاسيوم (KOH) بتركيز 6 مول/لتر. وتم إجراء التنشيط الفيزيائي ضمن نطاق درجات حرارة يتراوح بين 300، 350، 400، 450، و500 °م، ولمدد زمنية قدرها 1، 2، و3 ساعات. أُجري توصيف الكربون الأسود المستعاد باستخدام تقنية مطيافية الأشعة تحت الحمراء بتحويل فورييه(FTIR) ، وتحليل محتوى الرماد، ومطيافية الانبعاث البصري بالبلازما المقترنة حثيًا-ICP) (OES، واختبار بروناور–إيميت–تيلر(BET) ، ورقم امتزاز اليود (IAN). أظهرت نتائج إزالة المعادن انخفاضًا في محتوى الرماد من 11.36٪ إلى 8.05٪، كما تمّت إزالة عنصري الحديد ($Fe^{3+}$) والمغنيسيوم ($Mg^{2+}$). وعلى النقيض من ذلك، أدى التنشيط الفيزيائي إلى تعزيز ملحوظ في مسامية الكربون الأسود المستعاد، حيث بلغ أعلى سطح نوعي (BET) قيمة 188.52 م²/غ ورقم امتزاز يود بلغ 100 ملغ/غ عند درجة 450 °م لمدة 1–2 ساعة. كما أدت زيادة درجات الحرارة إلى انهيار المسام، خاصة عند 500 °م. تشير النتائج إلى أن درجة الحرارة المثلى والمدة المناسبة لعملية التنشيط الفيزيائي تُحسِّن من بنية الكربون الأسود المستعاد. ويسهم هذا الأمر في توسيع نطاق استخدام تقنيات المعالجة في تحسين البيئة، بما في ذلك معالجة مياه الصرف المحتوية على الأصباغ.

**الكلمات المفتاحية:** المعالجة البيئية، حمض الهيدروكلوريك، رقم امتزاز اليود، هيدروكسيد البوتاسيوم، الانحلال الحراري، المساحة السطحية.